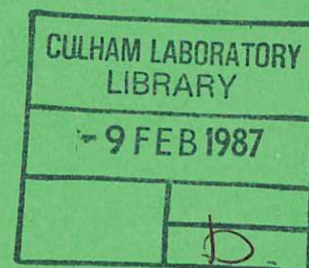UKAEA

Preprint

BUOYANCY-DRIVEN, TRANSIENT, TWO-DIMENSIONAL THERMO-HYDRODYNAMICS OF A MELT-WATER-STEAM MIXTURE

A. THYAGARAJA
D. F. FLETCHER

CULHAM LABORATORY
Abingdon, Oxfordshire
1986

BUOYANCY-DRIVEN, TRANSIENT, TWO-DIMENSIONAL THERMO-HYDRODYNAMICS OF A MELT-WATER-STEAM MIXTURE

by

A. Thyagaraja and D.F. Fletcher

Culham Laboratory, Abingdon, Oxon, OX14 3DB, UK

Abstract

In this paper we describe a finite difference code which has been developed to simulate two-dimensional multiphase mixing. The code models the dynamics and inter-component heat transfer of a hot liquid poured into a pool of cold volatile liquid. Predictions from the code are found to be in good agreement with experimental data. In addition, a quantitative measure of "mixing" has been devised and used to study the effect of parameters, such as ambient pressure, melt temperature and melt particle size, on mixing.

September 1986

1. Introduction

In this paper we describe a two-dimensional transient multiphase flow
code developed to model buoyancy-driven mixing processes which occur on
relatively slow timescales (~ 1 second). For example, we wish to model
the behaviour of a hot liquid when poured into a pool of cold vaporisable
liquid. This is a situation which may occur in certain industrial
processes [1], submarine volcanisms [2], and could arise during the
progression of accidents in nuclear reactors if core material melts and
pours into liquid coolant, (i.e. the coarse mixing stage of a steam
explosion) [3].

In earlier papers we described the development of a 1d, 2 component
[4] and a 1d, 3 component [5] finite difference code. In this paper we
use the same approach to develop a 2d, 3 component mixing code. As in our
earlier work the code allows the use of very general constitutive
relations for heat transfer and inter-phase momentum exchange.

The paper is organised as follows: in Section 2 the full set of
equations solved, together with the initial and boundary conditions needed
to completely specify the problem are given. In Section 3 the finite
difference scheme is outlined and in Section 4 the solution procedure is
described. Section 5 is devoted to a description of the form of the
constitutive relations used. In Section 6 we describe results obtained
from the code, including comparison with experimental data. In addition,
we describe a quantitative method for characterising coarse mixtures,

with steam explosion research in mind. Section 7 presents a discussion of the results obtained and conclusions.

2. Mathematical Formulation

We suppose, as in our earlier work [5], that three components are present. These are respectively the 'melt' (hot corium, for example), the 'liquid' phase of the coolant (we take this to be water at its saturation temperature) and the 'vapour' phase of the coolant (in our applications, steam). The flow velocities in the problems we shall be concerned with are small enough to allow the incompressible approximation: thus the mass densities ρ_M, ρ_W, ρ_S are taken to be constant. The flows take place under gravity in a circular cylinder of vertical height H and radius R. In contrast to our earlier papers, we consider variations in r, z and t. The model is decribed by the following eleven dependent variables:

$\alpha_M(r,z,t)$, $\alpha_W(r,z,t)$, $\alpha_S(r,z,t)$ — Volume fractions

$U_M(r,z,t)$, $U_W(r,z,t)$, $U_S(r,z,t)$ — Horizontal velocity components

$V_M(r,z,t)$, $V_W(r,z,t)$, $V_S(r,z,t)$ — Vertical velocity components

$p(r,z,t)$ — Common hydrostatic pressure

$H_M(r,z,t)$ — Melt specific enthalpy

For completeness, it should be mentioned that the constitutive

equations involve the melt temperature $T_M(r,z,t)$ which is related to H_M through an appropriate equation of state. Gravity is assumed to act vertically downwards and, as usual, we denote the acceleration due to gravity by g . As before [5], we introduce a reduced pressure

$$\bar{p}(r,z,t) = p(r,z,t) - \int_z^H g(\rho_M \alpha_M + \rho_S \alpha_S + \rho_W \alpha_W)dz$$

$$\equiv p(r,z,t) - \chi(r,z,t) \tag{2.1}$$

It follows that

$$\frac{\partial \bar{p}}{\partial z} = \frac{\partial p}{\partial z} + g(\rho_M \alpha_M + \rho_S \alpha_S + \rho_W \alpha_W) \tag{2.2}$$

However, it should be carefully noted that $\frac{\partial \bar{p}}{\partial r}$ is <u>not</u> related to $\frac{\partial p}{\partial r}$ in a simple manner.

The eleven dependent variables defined above are governed by the following equations:

$$\frac{\partial \alpha_M}{\partial t} + \frac{1}{r}\frac{\partial}{\partial r}(r\alpha_M U_M) + \frac{\partial}{\partial z}(\alpha_M V_M) = 0 \tag{2.3}$$

$$\frac{\partial \alpha_W}{\partial t} + \frac{1}{r}\frac{\partial}{\partial r}(r\alpha_W U_W) + \frac{\partial}{\partial z}(\alpha_W V_W) = \frac{\dot{m}_W}{\rho_W} \tag{2.4}$$

$$\frac{\partial \alpha_S}{\partial t} + \frac{1}{r}\frac{\partial}{\partial r}(r\alpha_S U_S) + \frac{\partial}{\partial z}(\alpha_S V_S) = \frac{\dot{m}_S}{\rho_S} \tag{2.5}$$

$$\alpha_S + \alpha_M + \alpha_W = 1 \tag{2.6}$$

$$\frac{\partial}{\partial t}(\rho_M \alpha_M U_M) + \frac{1}{r}\frac{\partial}{\partial r}(r\rho_M \alpha_M U_M{}^2) + \frac{\partial}{\partial z}(\rho_M \alpha_M U_M V_M)$$

$$= -\alpha_M \frac{\partial \bar{p}}{\partial r} - \alpha_M \frac{\partial \chi}{\partial r} + F_{MW}^r + F_{MS}^r \tag{2.7}$$

$$\frac{\partial}{\partial t}(\rho_M \alpha_M V_M) + \frac{1}{r}\frac{\partial}{\partial r}(r\rho_M \alpha_M U_M V_M) + \frac{\partial}{\partial z}(\rho_M \alpha_M V_M{}^2)$$

$$= -\alpha_M \frac{\partial \bar{p}}{\partial z} + g\alpha_M \alpha_W (\rho_W - \rho_M) + g\alpha_M \alpha_S (\rho_S - \rho_M)$$

$$+ F_{MW}^z + F_{MS}^z \tag{2.8}$$

$$\frac{\partial}{\partial t}(\rho_W \alpha_W U_W) + \frac{1}{r}\frac{\partial}{\partial r}(r\rho_W \alpha_W U_W^2) + \frac{\partial}{\partial z}(\rho_W \alpha_W V_W U_W)$$

$$= -\alpha_W \frac{\partial \bar{p}}{\partial r} - \alpha_W \frac{\partial \chi}{\partial r} + F_{WM}^r + F_{WS}^r + F_{W\dot{m}}^r \tag{2.9}$$

$$\frac{\partial}{\partial t} (\rho_W \alpha_W V_W) + \frac{1}{r} \frac{\partial}{\partial r} (r \rho_W \alpha_W U_W V_W) + \frac{\partial}{\partial z} (\rho_W \alpha_W V_W^2)$$

$$= - \alpha_W \frac{\partial \overline{p}}{\partial z} + g \alpha_W \alpha_M (\rho_M - \rho_W)$$

$$+ g \alpha_W \alpha_S (\rho_S - \rho_W) + F_{WM}^z + F_{WS}^z + F_{W\dot{m}}^z \qquad (2.10)$$

$$\frac{\partial}{\partial t} (\rho_S \alpha_S U_S) + \frac{1}{r} \frac{\partial}{\partial r} (r \rho_S \alpha_S U_S^2) + \frac{\partial}{\partial z} (\rho_S \alpha_S V_S U_S)$$

$$= - \alpha_S \frac{\partial \overline{p}}{\partial r} - \alpha_S \frac{\partial \chi}{\partial r} + F_{SM}^r + F_{SW}^r + F_{S\dot{m}}^r \qquad (2.11)$$

$$\frac{\partial}{\partial t} (\rho_S \alpha_S V_S) + \frac{1}{r} \frac{\partial}{\partial r} (r \rho_S \alpha_S U_S V_S) + \frac{\partial}{\partial z} (\rho_S \alpha_S V_S^2)$$

$$= - \alpha_S \frac{\partial \overline{p}}{\partial z} + g \alpha_S \alpha_M (\rho_M - \rho_S)$$

$$+ g \alpha_S \alpha_W (\rho_W - \rho_S) + F_{SM}^z + F_{SW}^z + F_{S\dot{m}}^z \qquad (2.12)$$

$$\frac{\partial}{\partial t} (\alpha_M \rho_M H_M) + \frac{1}{r} \frac{\partial}{\partial r} (r \alpha_M \rho_M H_M U_M) + \frac{\partial}{\partial z} (\alpha_M \rho_M V_M H_M)$$

$$= - Q_M^H \qquad\qquad (2.13)$$

The following comments relate to the above system and its practical applications:

(1) As in our previous work we assume that there are no sources or sinks of the melt in the solution domain (ie $\dot{m}_M \equiv 0$).

(2) We neglect condensation of steam (ie $\dot{m}_S \geqslant 0$) and assume that $\dot{m}_W + \dot{m}_S = 0$. Furthermore, $\dot{m}_W$ is taken to be given by

$$\dot{m}_W = - \alpha_W \alpha_M \rho_S \ \lambda(r,z,t) \qquad\qquad (2.14)$$

where the rate function λ must be calculated using the melt temperature $T_M(r,z,t)$ and constitutive relations to be specified later. It is enough to remark that λ will be non-negative. With these provisos, Equations (2.3) and (2.4) will be used later to advance α_M and α_W. α_S is then determined from Equation (2.6). For this procedure to be consistent, it is necessary (and sufficient!) that the 'elliptic constraint',

$$\frac{1}{r} \frac{\partial}{\partial r} \left(r(\alpha_M U_M + \alpha_W U_W + \alpha_S U_S) \right) + \frac{\partial}{\partial z} (\alpha_M V_M + \alpha_W V_W + \alpha_S V_S)$$

$$= \dot{m}_S \left(\frac{1}{\rho_S} - \frac{1}{\rho_W} \right) \quad . \quad\quad (2.15)$$

is satisfied.

Equation (2.15) is solved (using Newton's method) for the reduced pressure $\bar{p}$.

(3) The role of the reduced pressure and the 'potential' $\chi(r,z,t)$ requires explanation. The purpose of the decomposition (2.1) is to separate out the hydrostatic and the hydrodynamic components of the total pressure p. The potential χ represents the average hydrostatic pressure felt by the three components. It simplifies the vertical momentum equations (2.8), (2.10) and (2.12). The effective buoyancy forces in these equations have the characteristic property of cancelling in pairs. This feature was already noted in our 1-d treatment of the mixing problem [5]. However, in contrast to 1-d, there are new buoyancy-related radial forces appearing in Equations (2.7), (2.9) and (2.11), via the $\frac{\partial \chi}{\partial r}$ term. These forces are due in effect to the variation of the α's with r.

(4) The drag forces F_{MW}^r etc. have exactly the same general structure as in our 1-d simulations. The details are given in Section 5 on constitutive relations. It suffices for the present to note that,

$$F^r_{MW} = D^r_{MW} (\alpha_M, \alpha_W, \rho_M, \rho_W ..) (U_W - U_M)$$

$$F^r_{WM} = D^r_{WM} (\alpha_M, ...) (U_M - U_W)$$

where $D^r_{WM} \equiv D^r_{WM}$ etc. (thus ensuring $F^r_{MW} + F^r_{WM} = 0$)

$$F^r_{MS} = D^z_{MS} (V_S - V_M)$$

$$F^z_{SM} = D^z_{SM} (V_M - V_S)$$

$$D^z_{MS} = D^z_{SM} \quad \text{etc.}$$

(5) The evaporation reaction forces $F^z_{S\dot{m}}$ etc., are treated exactly the same as in our earlier work

ie., $F^z_{W\dot{m}} + F^z_{S\dot{m}} = 0$, $F^z_{S\dot{m}} = \dot{m}_S V_W$ and

$F^r_{W\dot{m}} + F^r_{S\dot{m}} = 0$, $F^r_{S\dot{m}} = \dot{m}_S U_W$

(6) The boundary conditions needed to solve the above system of equations consist of the following:

The solution domain is defined by, $0 \leqslant r \leqslant R$; $0 \leqslant z \leqslant H$.

(a) By symmetry, $U_M, U_W, U_S \equiv 0$ on $r = 0$.

(b) The boundaries at $r = R$ and $z = 0$ are 'impermeable':

thus $U_M = U_W = U_S = 0$ on $r = R$

$V_M = V_W = V_S = 0$ on $z = 0$.

(c) The boundary at $r = H$ is 'open'. It is assumed that H is large enough so that the flow at this boundary is 'developed'; ie., $U_M = U_W = U_S = 0$ on $z = H$. Conditions on the V's and α's cannot be totally arbitrary but must satisfy the following compatibility condition which follows from Eq.(2.15).

$$2\pi \int_0^R rdr \left\{ \alpha_M V_M + \alpha_W V_W + \alpha_S V_S \right\}_{z = H}$$

$$= 2\pi \int_0^R \int_0^H rdrdz \left\{ \dot{m}_S \left(\frac{1}{\rho_S} - \frac{1}{\rho_W} \right) \right\} \qquad (2.16)$$

Since $\dot{m}_S$ is always non-negative, it follows that the volumetric flux out of the system (the left hand side of Eq.(2.16)) must always be non-negative. As far as steam and water are concerned, we shall <u>always</u> treat $z = H$ as an <u>outflow</u> boundary. For water, this results in the following prescription: $V_W(r,H,t)$ is required to be obtained from the condition $\frac{\partial V_W}{\partial z}(r,H,t) = 0$. Typically this condition leads to outflow, $V_W(r,H,t) \geqslant 0$. If it should turn out that $V_W(r,H,t) \leqslant 0$, we set $\alpha_W(r,H,t) \equiv 0$, thus allowing no inflow of water. It is evident from this

that the global water occupancy defined by $\bar{\alpha}_W(t) = 2 \dfrac{\int_0^H \int_0^R r\,dr\,dz\,\alpha_W}{R^2 H}$ is a

non-increasing function of time. Thus, $0 < \bar{\alpha}_W(t) \leq \bar{\alpha}_W(0) < 1$ for all

t.

In the case of melt, there are two types of physically relevant

conditions. Firstly, we could consider the pure initial value problem in

which $\alpha_M(r,z,0)$ and the melt velocity distributions within the solution

domain are prescribed at $t = 0$. In this case, $z = H$ is treated as an

outflow boundary and $\dfrac{\partial V_M}{\partial z}(r,H,t) = 0$. Thus, the treatment of melt is

exactly the same as water. The global melt occupancy, $\bar{\alpha}_M(t) =$

$2 \dfrac{\int_0^H \int_0^R r\,dr\,dz\,\alpha_M}{R^2 H}$ is non-increasing and satisfies $0 < \bar{\alpha}_M(t) \leq \bar{\alpha}_M(0) < 1$.

Secondly, we could consider Stefan-type problems in which the boundary

$z = H$ is divided into two segments: $0 < r \leq a_{in}$ is an <u>inlet</u> region in

which $V_M(r,H,t)$ is prescribed and given a <u>negative</u> velocity for certain

time intervals. $\alpha_M(r,H,t) \neq 0$ (and is specified explicitly) is also

imposed for these intervals in the inlet region. This corresponds to a

melt <u>injection</u>. For $a_{in} < r \leq R$, the treatment is the same as for an

outlet boundary. In these problems, it is no longer true that $\bar{\alpha}_M(t)$ is

non-increasing. However, the melt injection is compatible with the

incompressibility assumption (ie., ρ_M is independent of space and time

variation) only as long as $\bar{\alpha}_M(t) < 1$ is satisfied. In practical

problems, this is <u>always</u> the case. Finally, having fixed on the

appropriate boundary conditions on V_W and V_M on $z = H$, $V_S(r,H,t)$ is

determined from (2.16) together with the condition $\dfrac{\partial V_S}{\partial r} \equiv 0$ on $z = H$.

(7) The mathematical specification of the problem is completed by

prescribing, via suitable constitutive equations, the following quantities

as functions of dependent variable or external parameters:

    (i)   The rate function λ.

    (ii)   The drag functions D_{MW}^r etc.

    (iii)   The melt caloric equation of state relating H_M to T_M at

           constant ρ_M.

    (iv)   The heat transfer functions (radiation, film-boiling etc.)

           relating to Q_M^H.

These constitutive relations are discussed in Section 5 which also deals

with certain auxiliary parameters such as length-scales.

    Although strict mathematical proof is lacking, the above system is

believed to be well-posed and leads to a unique solution to the

initial-boundary value problem. Numerical evidence suggests strongly that

for physically relevant parameters, the solution depends smoothly on the

initial data and the parameters for all times.

3. Finite-Difference Formulation

The non-linear equation system Eq.(2.3)-(2.13) which determines the temporal evolution and spatial variation of the eleven state variables must be solved numerically. The reformulation of this system as a set of finite-difference equations on a suitable mesh is the objective of the present section. The principles of the method have already been established in our 1-d work [4], [5]. For this reason, the description here is kept brief and restricted to the changes necesitated by adding an extra spatial dimension.

Figure 1 shows the cross-section (vertical) of the cylindrical vessel of radius R and height H. The solution domain in the (r,z) plane through the central axis EF is the rectangle EDCF. For illustrative purposes, a 4 × 9 rectangular grid is sketched (we use NR x NZ for the general case). The radial and vertical mesh sizes (Δr and Δz respectively) are taken uniform. The index i runs from 1 to 4 and labels the ith radial interval while j runs from 1 to 9 and labels the jth vertical interval from the bottom upwards.

A typical "continuity cell" PQRS is shown with its central point (i,j). It is evident that $r_i = (i-1)\Delta r + \frac{\Delta r}{2}$ while $z_j = (j-1)\Delta z + \frac{\Delta z}{2}$. The following quantities are "stored" at (i,j):

The volume fractions: $\alpha(r_i, z_j, n\Delta t) \equiv \left(\alpha_{i,j}^n\right)_{M,W,S}$

The reduced pressure: $\bar{p}(r_i, z_j, n\Delta t) \equiv \bar{p}_{i,j}^n$

The potential χ: $\qquad\qquad \chi(r_i, z_j, n\Delta t) \equiv \chi_{i,jM}^n$

The Melt enthalpy: $\qquad\qquad H_M(r_i, z_j, n\Delta t) \equiv (H_{i,j}^n)_M$

The vertical U-velocities corresponding to (i,j) are stored at (i + ½ j) (ie., the mid-point of QR) while the V-velocities are at (i, j + ½). It should be noted carefully that the radial boundaries at $r = 0$ and $r = R$, correspond to U-velocity storage locations (thus enabling these to be set to zero). The bottom of the vessel, $z = 0$, corresponds to V storage locations. The impermeability condition is simply, $V = 0$. The treatment at ED is described later. With these conventions, it is evident that

$$U(r_{i+\frac{1}{2}}, z_j, n\Delta t) \equiv \left(U_{i,j}^n\right)_{M,W,S}$$

$$V\left(r_i, z_{j+\frac{1}{2}}, n\Delta t\right) \equiv \left(V_{ij}^n\right)_{M,W,S}$$

The finite-difference forms of Equations (2.3), (2.4) and (2.13) are simply derived by multiplying them by the volume element $rdrdz$ and integrating over PQRS (ie., typical continuity cell).

The fluxes appropriate to the cell walls involve the corresponding velocity components and "upwind" interpolated α's and H_M. It is convenient in this context to refer to QR as the r_+ face of the cell whilst PS is the r_- face; PQ is the z_+ face and so on. For example, the flux of melt out of the r_+ face at (i,j) corresponding to $t = n\Delta t$ is

$$\left(F_r^+\right)_M \equiv \left(r_i + \frac{\Delta r}{2}\right)\Delta z \left(U_{i,j}^n\right)_M \left(\alpha_M^n\right)_+$$

(3.1)

where $\quad \left(\alpha_M^n\right)_+ \equiv \left(\alpha_{i,j}^n\right)_M \quad$ if $\quad \left(U_{i,j}^n\right)_M > 0$

$$\equiv \left(\alpha_{i+1,j}^n\right)_M \quad \text{if} \quad \left(U_{i,j}^n\right)_M < 0.$$

More concisely,

$$\left(\alpha_M^n\right)_+ = \left(\alpha_{i,j}^n\right)_M \theta_+ + \left(\alpha_{i+1,j}^n\right)_M \left(1-\theta_+\right)$$

(3.2)

where $\quad \theta_+ = 1 \quad$ if $\quad \left(U_{i,j}^n\right)_M > 0 \quad$ and zero, otherwise.

In this method, the convective terms are treated explicitly (ie., Eq.(2.3) for example, is forward differenced in time). If $\left(\alpha_{i,j}^n\right)_M$ and $\left(U_{i,j}^n\right)_M$, $\left(V_{i,j}^n\right)_M$ are known, $\left(\alpha_{i,j}\right)_M$ can be calculated. The use of upwinding ensures that the transformation matrix linking $\alpha_{i,j}^{n+1}$'s to the $\alpha_{i,j}^n$'s is positive faithful [4] when the Courant conditions $\frac{\Delta r}{\Delta t}$, $\frac{\Delta z}{\Delta t} > \underset{i,j}{\text{Max}}\left(\left|U_{i,j}^n\right|,\right.$ $\left.\left|V_{i,j}^n\right|\right)$ are satisfied.

The treatment of Equations (2.4) and (2.13) is exactly the same as far as the convective terms are concerned. The sink terms are handled as in [5].

Recall that $\dfrac{\dot{m}_W}{\rho_W} = - \alpha_W \alpha_M \dfrac{\rho_S}{\rho_W} \lambda.$ In finite-difference form this is

written as

$$\int_{PQRS} rdrdz \frac{\dot{m}_W}{\rho_W} \equiv - r_i \Delta r \; \Delta z \left(\alpha_{i,j}^{n+1}\right)_W \frac{\rho_S}{\rho_W} \lambda_{i,j}^n \left(\alpha_{ij}^{n+1}\right)_M \qquad (3.3)$$

In Eq.(3.3) recall that $\left(\alpha_{i,j}^{n+1}\right)_M$ will be available in store since the melt equation is solved first. $\lambda_{i,j}^n$ is calculated purely from values of quantities at $t = n \, \Delta t$. It is then apparent that the coefficient of $\left(\alpha_{i,j}^{n+1}\right)_W$ in the finite-difference form of Eq.(2.4) is simply

$$r_i \Delta r \; \Delta z \; \left\{ 1 + \frac{\rho_S}{\rho_W} \lambda_{i,j}^n \Delta t \left(\alpha_{i,j}^{n+1}\right)_M \right\} \; .$$

For accuracy, Δt must be small enough for the second term in the braces to be a small relative to unity. In this event, $\left(\alpha_{i,j}^{n+1}\right)_W$ will always remain non-negative and less than unity.

Q_M^H is always a flux of enthalpy out of the melt due to various transport processes. In Eq.(2.13) it is finite-differenced as follows:

$$\int_{PQRS} rdrdz \; Q_M^H \equiv \left(H_{i,j}^{n+1}\right)_M r_i \Delta r \; \Delta z \left(Q_M^H\right)_{i,j}^n \Big/ \left(H_{i,j}^n\right)_M . \qquad (3.4)$$

The multiplier of $\left(H_{i,j}^{n+1}\right)_M$ in the finite-difference form of (2.13) is then

- 15 -

$$r_i \Delta r \, \Delta z \, \left\{ 1 + \left(Q_N^H\right)_{i,j}^n \, \frac{\Delta t}{H_{i,j}^n} \Big)_M \right\} \tag{3.5}$$

Δt must satisfy the accuracy requirement

$$\Delta t \; \tau_{i,j}^n \; \ll \; 1 \tag{3.6}$$

where the 'cooling' time is defined by, $\quad \tau_{i,j}^n \equiv \dfrac{\left(H_{i,j}^n\right)_M}{\left(Q_M^H\right)_{i,j}} \tag{3.7}$

4. Solution Scheme

The present section is concerned with the iterative technique developed to solve the equations (2.3)-(2.13). We suppose that at t = n Δt, we have in store the eleven dependent variables at the appropriate grid locations. The velocity fields and the pressure are required to satisfy the finite-difference form of Eq.(2.15). We assume this to be the case and are interested in evaluating the fields at t = (n+1) Δt. In the previous section, it was shown how the values of the α's and H_M are obtained explicitly at t = (n+1) Δt and the mesh points (i,j).

It will be recalled that this calculation does not need any knowledge (explicit) of the pressure or any other fields at t = (n+1) Δt. Once this calculation is performed, we have $\alpha_{i,j}^{n+1}$'s in store. The task is to solve the finite-difference forms of the six momentum equations (2.7)-(2.12) and (2.15) to obtain self-consistently $\bar{p}_{i,j}^{n+1}$, $\left(U_{i,j}^{n+1}\right)_{M,W,S}$, $\left(V_{i,j}^{n+1}\right)_{M,W,S}$. Since

the equations are non-linear, and since the time-differencing of the convective terms is implicit (ie., involves quantities like $\frac{1}{2}(U_{i,j}^{n+1} + U_{i,j}^{n})$, for example), an iteration scheme is involved. The scheme, to be described below, resembles the one described in our one-dimensional analysis [5]. However, as will be apparent, it is much more powerful and stable than the earlier one and computationally simpler and faster. To explain its features, some new notation is needed. If $\Psi_{i,j}^{n}$ represents any property at $t = n\Delta t$ associated with (i,j) we need two more indices:

$$\left(\Psi_{i,j}^{n}\right)_{\sigma}^{\nu}, \quad \text{where} \quad \nu = 1,2,\ldots$$

is the 'iteration' index while $\sigma = M(1), W(2), S(3)$ is the 'species' index. For example $\left(V_{i,j}^{n+1}\right)_{1}^{2}$ means the second approximation to $\left(V_{i,j}^{n+1}\right)_{M}$. By convention, $\left(\Psi_{i,j}^{n+1}\right)_{\sigma}^{1} \equiv \left(\Psi_{i,j}^{n}\right)_{\sigma}$ for all n, i,j and σ.

Let us consider the iteration scheme for obtaining $\left(U_{i,j}^{n+1}\right)_{\sigma}$, $\left(V_{i,j}^{n+1}\right)_{\sigma}$, $\bar{p}_{i,j}^{n+1}$ in outline. The details are described and understood best <u>after</u> the structure of the scheme has been exposed. Suppose then that we have in store the following arrays: $\left(\alpha_{i,j}^{n}\right)_{\sigma}$ $\left(\alpha_{i,j}^{n+1}\right)_{\sigma}$ $\left(V_{i,j}^{n}\right)_{\sigma}$ $\left(p_{i,j}^{n}\right)_{\sigma}$, $H_{M_{i,j}}^{n+1}$, $H_{M_{i,j}}^{n}$ and $\left(\bar{p}_{i,j}^{n+1}\right)^{\nu}$, $\left(V_{i,j}^{n+1}\right)_{\sigma}^{\nu}$, $\left(U_{i,j}^{n+1}\right)_{\sigma}^{\nu}$ for some value of ν. In order to calculate $\left(V_{i,j}^{n+1}\right)_{\sigma}^{\nu+1}$, $\left(U_{i,j}^{n+1}\right)_{\sigma}^{\nu+1}$, $\left(\bar{p}_{i,j}^{n+1}\right)^{\nu+1}$ we proceed as follows:

Step 1:   The V-momentum equations (2.8), (2.10), (2.12) are set up in the

manner indicated later and solved to give $\left(v_{i,j}^{n+1}\right)_\sigma^{\nu+1}$. The solution does

not involve either a tridiagonal matrix algorithm or an ADI type inversion

involving the entire i,j mesh. Instead, an implicit treatment of the

drag terms results in the inversion of a three-by-three symmetric,

diagonally dominant matrix at <u>each</u> (i,j) point where the V's are

stored.

Step 2:   The U-momentum equations (2.7), (2.9), (2.11) are set up and

solved exactly as in Step 1 above to obtain $\left(u_{i,j}^{n+1}\right)_\sigma^{\nu+1}$.

Step 3:   Equation (2.15) is integrated over r for fixed z (ie.,

keeping j fixed, the finite-difference form of (2.15) is summed over

i). The pressure $\left(\bar{p}_{i,j}^{n+1}\right)^{\nu+1}$ is split into three pieces as follows:

$$\left(\bar{p}_{i,j}^{n+1}\right)^{\nu+1} \equiv \left(\bar{p}_{i,j}^{n+1}\right)^{\nu} + \Delta\bar{p}_j^{\nu} + \delta\bar{p}_{i,j}^{\nu} \qquad\qquad (4.1)$$

where $\displaystyle\sum_{i=1}^{NR} \delta\bar{p}_{i,j}^{\nu} = 0$ by definition.

If j runs from 1 to NZ, the above procedure generates NZ

equations for $\Delta\bar{p}_j^{\nu}$ j = 1,..NZ. By virtue of Eq.(2.16), one of these

equations is redundant. Indeed, since pressure in the present context is

a 'relative variable', we may set $\Delta\bar{p}_{NZ}^{\nu} \equiv 0$ and consider the (NZ-1)

equations generated from Eq.(2.15). These will be seen to have a
diagonally dominant tri-diagonal structure and are solved by the
appropriate matrix algorithm to obtain the pressure level corrections
$\Delta \bar{p}_j^{\nu}$.

Step 4: In this step, we seek to determine $\delta \bar{p}_{i,j}^{\nu}$ by setting up, for
each j, NR finite-difference equations obtained by integrating
Eq.(2.15) over each continuity cell. The matrix which links $\delta \bar{p}_{i,j}^{\nu}$ is
tri-diagonal whilst the sources are the continuity errors at each (i,j)
location. Only NR-1 of these equations are linearly independent.
However, the condition $\sum_{i=1}^{NR} \delta \bar{p}_{i,j}^{\nu} = 0$ ensures that all the $\delta \bar{p}$'s are
determinate.

It is apparent that at the conclusion of Step 4, we have calculated
$\left(\bar{p}_{i,j}^{n+1} \right)^{\nu+1}$, $\left(v_{i,j}^{n+1} \right)_{\sigma}^{\nu+1}$, $\left(U_{i,j}^{n+1} \right)_{\sigma}^{\nu+1}$ and (hopefully!) reduced the local (and
global) continuity errors in the finite-difference forms of Eq.(2.15).
The iterative procedure is continued until a non-dimensional measure of
these errors is reduced to a pre-assigned level.

Steps 3 and 4 are quite straight-forward extensions to two dimensions
of the one-dimensional pressure correction scheme described in earlier
papers. The really novel element consists of the finite-difference
approach to Steps 1 and 2. It suffices to give an account of the method
for Step 1 as it applies with only trivial modification to Step 2.

Let us integrate Eq.(2.8) over a V momentum cell at (i,j) and over a small time Δt.   We then get,

$$\rho_M\left(\alpha_{i,j+\frac{1}{2}}^{n+1}\right)_M \left(v_{i,j}^{n+1}\right)_M = \rho_M\left(\alpha_{i,j+\frac{1}{2}}^{n}\right)_M \left(v_{i,j}^{n}\right)_M + \Delta t\left(s_{i,j}\right)_M \qquad (4.2)$$

$$\alpha_{i,j+\frac{1}{2}}^{n} \equiv \frac{1}{2}\left(\alpha_{i,j}^{n} + \alpha_{i,j+1}^{n}\right) \quad \text{etc.}$$

The term $\left(s_{i,j}\right)_M$ comprises many contributions. Firstly, let us consider the buoyancy terms. These have the following integral forms:

$$\int_{(i,j)} g\alpha_M\alpha_W\left(\rho_W - \rho_M\right) \text{d volume d time} \; / \int_{(i,j)} \text{d volume}$$

$$\equiv g\left(\rho_W - \rho_M\right)\Delta t \; \left(\alpha_M\alpha_W\right)_{i,j+\frac{1}{2}}^{n+\frac{1}{2}} \qquad (4.3)$$

where $\left(\alpha_M\alpha_W\right)_{i,j+\frac{1}{2}}^{n+\frac{1}{2}} = \frac{1}{8}\left[\left(\left(\alpha_{i,j}^{n+1}\right)_M + \left(\alpha_{i,j}^{n}\right)_M\right)\left(\left(\alpha_{i,j}^{n+1}\right)_W + \left(\alpha_{i,j}^{n}\right)_W\right)\right.$

$$\left. + \left(\left(\alpha_{i,j+1}^{n+1}\right)_M + \left(\alpha_{i,j+1}^{n}\right)_M\right)\left(\left(\alpha_{i,j+1}^{n+1}\right)_W + \left(\alpha_{i,j+1}^{n}\right)_W\right)\right]$$

The integrals are space-time centred. As they do <u>not</u> involve v_σ^{n+1}'s, they are explicit sources.

Next, consider the $\frac{\partial \bar{p}}{\partial z}$ term. In Step 1, $\bar{p}_{i,j}^{v+1}$ is not known as yet. Thus, we use the following formula:

$$\int\limits_{(i,j)} \alpha_M \frac{\partial \bar{p}}{\partial z} \, d \text{ volume } d \text{ time } / \int\limits_{(i,j)} d \text{ volume}$$

$$= - (\frac{\Delta t}{\Delta z})(\alpha_{i,j+\frac{1}{2}}^{n+\frac{1}{2}})_M \; (\bar{p}_{i,j+1}^{\nu} - \bar{p}_{i,j}^{\nu}) \tag{4.4}$$

This too is an explicit source term in Eq.(4.2). Thirdly, we discuss the terms F_{MW}^z and F_{MS}^z. For example, the term F_{MW}^z has the general form,

$$F_{MW}^z \equiv D_{MW}^z \; (V_W - V_M) \tag{4.5}$$

where the coefficient D_{MW}^z is non-negative and is a function of ρ_σ, α_σ and U_σ, V_σ. (See Section 5 for the exact formulae used.) In order to treat this term purely implicitly, we set

$$\int\limits_{(i,j)} F_{MW}^z \, d \text{ volume } d \text{ time } / \int\limits_{(i,j)} d \text{ volume}$$

$$\equiv \Delta t (D_{MW}^z)_{i,j+\frac{1}{2}}^{n+\frac{1}{2}} ((V_{i,j}^{n+1})_W - (V_{i,j}^{n+1})_M) \tag{4.6}$$

In Eq.(4.6) $(D_{MW}^z)_{i,j+\frac{1}{2}}^{n+\frac{1}{2}}$ means it is space-time centred (ie., its arguments are evaluated at these locations and substituted in the assumed functional form for D_{MW}^z). The above treatment leads to Eq.(4.2) taking the form of a linear-inhomogeneous equation involving $(V_{i,j}^{n+1})_\sigma$. The last term to be discussed is the convective momentum transport term in Eq.(2.8). The integral form of this is given by,

$$\int_{(i,j)} - \left\{ \frac{1}{r} \frac{\partial}{\partial r}(r \rho_M \alpha_M U_M V_M) + \frac{\partial}{\partial z}(\rho_M \alpha_M V_M^2) \right\} \text{d volume d time}$$

$$\div \int_{(i,j)} \text{d volume} = -\frac{\Delta t}{r_i \Delta r \Delta z} \left\{ \begin{array}{l} (\text{z-Flux of } V_M)_+ - \\ (\text{z-Flux of } V_M)_- \\ +(\text{r-Flux of } V_M)_+ - \\ (\text{r-Flux of } V_M)_- \end{array} \right\}$$

$$(4.7)$$

The fluxes are evaluated using upwind differencing. The expression on the right of Eq.(4.7) takes the general form,

$$- A_0 (V_{i,j}^{n+1})_M + A_{z+} (V_{i,j+1}^{n+1})_M + A_{z-}(V_{i,j-1}^{n+1})_M$$

$$+ A_{r+} (V_{i+1,j}^{n+1})_M + A_{r-}(V_{i-1,j}^{n+1})_M$$

where the coefficients A_0, A_{z+}, A_{z-}, A_{r-}, A_{r+}, are all non-negative

Putting the above results together, Eq.(4.2) takes the following form

$$(V_{i,j}^{n+1})_M \left\{ \rho_M (\alpha_{i,j+\frac{1}{2}}^{n+1})_M + \Delta t (D_{MW}^{z})_{i,j+\frac{1}{2}}^{n+\frac{1}{2}} + \Delta t (D_{MS}^{z})_{i,j+\frac{1}{2}}^{n+\frac{1}{2}} + A_o \right\}$$

$$+ (V_{i,j}^{n+1})_W (\,..\,) + (V_{i,j}^{n+1})_S (\,..\,)$$

$$= A_{z+} (V_{i+1j}^{n+1})_M + \cdots$$

$$+ \rho_M (\alpha_{i,j+\frac{1}{2}}^{n})_M (V_{i,j}^{n})_M$$

$$+ \Delta t (S_{i,j}^{*})_M \qquad\qquad (4.8)$$

In equation (4.8) $(S_{i,j}^{*})_M$ includes 'explicit' terms such as the buoyancy and pressure force terms. It is noteworthy that Eq.(4.8) formally couples $(V_{i,j}^{n+1})_M$ to $(V_{i\pm1,\underline{j}\pm1}^{n+1})_M$. In so far as the latter are not boundary values, the convective momentum flux links $(V_{i,j}^{n+1})_M$ with its near neighbours. Bearing in mind that (4.8) and its analogues derived by a similar process from equations (2.10) and (2.12) have to be solved iteratively, we set in equation (4.8) (and its analogues) all the velocities on the right hand side to be the values at the νth iteration. Thus $A_{+}(V_{i+1j}^{n+1})_M$ (for example) becomes $A_{+}(V_{i+1j}^{n+1})_M^{\nu}$.

It is plain (after a little algebraic re-arrangement) that at each (i,j) we have the following set of linear, inhomogeneous equations.

$$\sum_{\sigma^1=1}^{3} A^{(i,j)}_{\sigma\sigma^1} (V^{n+1}_{i,j})^{\nu+1}_{\sigma^1} = \bar{S}^{(i,j)}_{\sigma} \quad \sigma = 1,2,3. \tag{4.9}$$

This linear system has been constructed to have the following properties:

1) $\bar{S}^{(i,j)}_{\sigma}$ are functions of $(\alpha^n_{i,j})_{\sigma}$, $(\alpha^{n+1}_{i,j})_{\sigma}$, $(U^n_{i,j})_{\sigma}$, $(V^n_{i,j})_{\sigma}$, $(U^{n+1}_{i,j})^{\nu}_{\sigma}$, $(V^{n+1}_{i,j})^{\nu}_{\sigma}$, $\bar{p}^{\nu}_{i,j}$ and geometrical factors.

2) $A^{(i,j)}_{\sigma\sigma}$ for $\sigma = 1,2,3$ are non-negative.

3) $A^{(i,j)}_{\sigma\sigma^1} = A^{(i,j)}_{\sigma^1\sigma} < 0$ for $\sigma \neq \sigma^1$.

4) The $A^{(i,j)}$ matrix is diagonally dominant.

These properties are consequences of the structure of the inertial and drag terms (in particular, Newton's third law). It follows that given the values of all fields at $n\Delta t$ at the νth iteration, $(V^{n+1}_{i,j})^{\nu+1}_{\sigma}$ can be calculated at every point (i,j). The treatment of the U-equations is similar. Furthermore, there is no special difficulty in handling the evaporation reaction forces. The velocity fields $(U^{n+1}_{i,j})^{\nu+1}_{\sigma}$, $(V^{n+1}_{i,j})^{\nu+1}_{\sigma}$ calculated by this procedure are functions of $\bar{p}^{\nu}_{i,j}$. They will not necessarily satisfy the integral form of Eq.(2.15). The pressure correction equations described in Steps 3 and 4, are derived as in our one-dimensional treatment by relating $\Delta\bar{p}^{\nu}_{j}$ and $\delta p^{\nu}_{i,j}$ to $(\delta U^{n+1}_{i,j})^{\nu+1}_{\sigma}$.

$(\delta v_{i,j}^{n+1})_{\sigma}^{\nu+1}$ via a linearized, 'diagonal' approximation derived from equation (4.9).

Thus

$$(\delta v_{i,j}^{n+1})_{\sigma} = \frac{1}{A_{\sigma\sigma}^{(i,j)}} \frac{\delta \bar{s}^{(i,j)}}{\delta \bar{p}_{i,j}^{\nu}} \left\{ \Delta \bar{p}_{j}^{\nu} + \delta \bar{p}_{i,j}^{\nu} \right\}$$

$$+ \frac{1}{A_{\sigma\sigma}^{(i,j)}} \frac{\partial \bar{s}^{-(i,j)}}{\partial \bar{p}_{i,j+1}^{\nu}} \left\{ \Delta \bar{p}_{j+1}^{\nu} + \delta \bar{p}_{i,j+1}^{\nu} \right\} \qquad (4.10)$$

Expressions such as (4.10) lead to suitable tridiagonal systems for $\Delta \bar{p}_{j}^{\nu}$ and $\delta \bar{p}_{i,j}^{\nu}$. Solution of these (as described in Steps 3 and 4) lead to $\bar{p}_{i,j}^{\nu+1}$.

Although apparently complicated, the above procedure is more efficient than the scheme used in our one-dimensional simulations. The great physical importance of the drag forces between the species is fully taken into account and leads to a remarkable degree of numerical stability. The code has been run deliberately in a one-dimensional mode. The results agree to four or five significant figure accuracy with those obtained from the quite different 1-d code. The comparison problems include purely buoyancy driven ones ($\dot{m}_{s} \equiv 0$) and those in which there is a very large steam production. Purely two dimensional buoyancy driven flows have also been calculated with the 2-d code to check qualitative behaviour of the solutions for long times and stability. In all cases tested so far, the 2-d code has proved to be stable and as accurate as can be

expected. Grid refinement studies show acceptable convergence behaviour while realistic simulations demonstrate that even long time behaviour of global quantities depends smoothly on the initial conditions.

5.   Constitutive Relations

In this section the constitutive relations used to model inter-phase drag and heat transfer will be described. Recall that the drag force on species i by species j is denoted by

$$F_{i,j} = D_{i,j} \left(\underline{V}_j - \underline{V}_i \right) \tag{5.1}$$

In this work the drag law proposed by Harlow and Amsden [6] has been used, so that

$$D_{i,j} = \frac{3}{4} \alpha_i \alpha_j \rho_i \rho_j C_{D_{i,j}} \frac{L_i L_j}{(\rho_i L_j + \rho_j L_i)} \left(\frac{1}{L_i} + \frac{1}{L_j} \right)^2 \left| V_j - V_i \right| \tag{5.2}$$

where $C_{D_{i,j}}$ is the coefficient between phases i and j

L_i, L_j are the length-scales of phases i and j.

There is little physical justification for the above form of $D_{i,j}$ other than that it satisfies the necessary symmetry requirements and takes the correct limiting form as either phase becomes very dilute [5]. In the present work the length-scales for each phase are assumed to be constant. Improved modelling in this area is in progress.

The mass production rate of vapour was expressed in the general form

$$\dot{m}_S = \alpha_W \alpha_M \rho_S \lambda \qquad (5.3)$$

and it is required to derive an expression for λ. Assuming the melt is in the form of spherical particles with diameter L_M, then there are $\alpha_M/\frac{1}{6} \pi L_M^3$ particles per unit volume and if q is the heat flux per unit area from a particle, the total heat transfer rate per unit volume, Q, is given by

$$Q = 6q \; \alpha_M/L_M \qquad (5.4)$$

Clearly the production rate λ must depend on the value of α_W; if there is no water present Q must be zero. For simplicity and in the absence of data to the contrary we have assumed that a fraction $\alpha_W Q$ of the transferred energy produces steam and that the remainder is transferred between melt particles (in the present formulation the steam cannot be superheated and no heat is lost to the vessel walls). Thus the sink term in the enthalpy equation (2.13) is given by

$$Q_M^H = 6q \; \alpha_M \alpha_W/L_M \qquad (5.5)$$

Since the water is saturated and the steam produced is not superheated

$$\dot{m}_S = Q_M^H/h_{fg} \qquad (5.6)$$

where h_{fg} is the latent heat of vaporisation. Comparison of equation

- 27 -

(5.6) with equation (5.3) shows that

$$\lambda = 6q/L_M h_{fg} \rho_S \qquad (5.7)$$

Heat transfer was assumed to be by radiation and film boiling and q was expressed as

$$q = h\left(T_M - T_W\right) \qquad (5.8)$$

where h is the appropriate heat transfer coefficient. T_W is given by the saturation condition. The melt temperature was obtained from the enthalpy via the use of a suitable caloric equation. For example, if the melt freezes at a temperature T_f and the enthalpies of the solid and liquid at this temperature are denoted by H_S and H_L respectively, then

$$
\begin{aligned}
T_M &= H_M/C_{pS} + T_W & H_M &< H_S \\
&= T_f & H_S &\leqslant H_M \leqslant H_L \qquad (5.9) \\
&= T_f + \left(H_M - H_L\right)/C_{pL} & H_M &> H_L
\end{aligned}
$$

where we have assumed $H_M(T_W) = 0$ and C_{pL} and C_{pS} (the specific heat capacities for the liquid and solid melt phases, respectively) are independent of T_M.

The above description gives the particular forms of the constitutive relations used for the calculations presented in section 6. However, the

code is written in a completely general way which can be easily modified to explore the effect of other possible closure relations.

6.   Model Results

In this section we present results obtained from the two-dimensional mixing code when it was used to model an actual mixing experiment, and to scope the effect of vapour production on mixing.

6.1. Comparison of Code Results with Experimental Data

The code was used to simulate a 2d mixing experiment (CWTI-9) carried out at Argonne National Laboratory [7]. In this experiment molten corium was injected into a deep pool of water and the evolution of the system was examined. A detailed description of the experiment is given in reference 7, but the main features will be summarised here for clarity.

(i) The experiments were carried out in a cylindrical vessel 106 mm in radius and 511 mm high. This was represented by a 10 × 10 finite difference grid in the simulation. The vessel was initially filled to a depth of 320 mm with water at 367 K. Except for a melt injection orifice the vessel was sealed at the top. An expansion pipeway was fitted into the side of the vessel leading to an expansion tank with a volume of 1.4 m^3. The experimental geometry is illustrated in Figure 2. This tank was used to collect the melt and water "blown out" of the mixing vessel. The tank was heated above the saturation temperature of the steam so that the pressure in the expansion vessel could be used as a measure of the mass of steam produced in the mixing process. In the present simulation

we assume that the top of the mixing vessel is open, and determine the mass of steam water and melt ejected from the vessel. Thus the present simulation can be expected to over-predict the loss of water and melt compared with the experiment.

(ii) The corium, composed of 60% UO_2, 16% ZrO_2, and 24% stainless steel, was injected into the vessel as a jet with a diameter of 22 mm and an initial velocity of 3.7 m/s on entry into the water pool. The melt injection was in two stages: a well-defined jet with a flow-rate of 9.6 kg/s for the first 0.22s; followed by a 'multi-globule' pour with a flow-rate of 0.45 kg/s for $0.45s \leqslant t \leqslant 0.9s$. For the chosen finite difference mesh only the cell at the centre of the vessel allowed melt inflow. For the first pour the melt volume fraction at the top of the vessel was set to unity and for the second pour it was set to 6%. In both cases an initial velocity of ~ 3.1 m/s was used. A total corium mass of 2.39 kg was injected.

(iii) The corium was initially in liquid form at a temperature of 3080 K. The liquidus temperature of the oxidic phase was 1730 K. For the present calculations it was assumed that freezing took place at 2923 K at which temperature the latent heat (3.44×10^5 J/kg) was released. A value of 625 J/kg K was used for the corium specific heat, providing a suitable caloric equation to relate the melt enthalpy and temperature. Heat transfer was assumed to be by blackbody radiation and convective film boiling (the correlation proposed by Witte [8] was used). The steam production rate was weighted by a factor α_W to allow for the reduction in heat transfer when little water is present, for example, due to reduced absorption of radiation (see section 5 for further details).

(iv) All length-scales were assumed to be fixed. The water and steam length-scales were set equal to the vessel radius. The only justification for these assumptions is at present heuristic. The melt length-scale was a parameter of the calculation. At the end of the experiment the median particle size was 0.78 mm. For the present calculations the most suitable single length-scale to describe a distribution of particle sizes is the Sauter mean diameter [9], since this gives the correct value of the volume to surface area ratio. Assuming the particle size to be Lognormal [10] the Sauter mean diameter was estimated to be 2.7 mm. Thus we decided to perform simulations for particle sizes of 1 mm, 2 mm, and 3 mm.

(v) All the drag coefficients were set equal to 0.2 as this value was found to give the best agreement with experiment in our previous work [5].

(vi) A time-step of 5×10^{-6}s was used for the simulation with 1 mm particles and a time-step of 10^{-5}s was used for the simulations with 2 mm and 3 mm particles. Values this small were required to ensure that the large vapour production rate (cf. Eq. (3.3)) was modelled accurately. The calculations were carried out to a final time of 1.5 seconds, at which time most of the melt had settled into the base of the vessel to form a debris bed.

In the experiment the initial corium pour was observed to enter the water surface as a well-formed jet and to form a displacement crater and splash wave. Within 10 ms of the melt entering the water, the water pool was observed to undergo a dramatic boilup, essentially filling the entire

available cover gas volume. All these effects were observed in the simulation.

Figures 3(a) and 3(b) show the calculated volume fractions, for the case of 2 mm particles, at times of 0.1s and 0.2s, respectively. The Figures show that the melt jet spreads out very little as it falls through the steam and water. When the melt jet reaches the vessel bottom melt spreads out along the vessel base. At t = 0.1s the Figure shows that the water has been pushed aside by the melt forming a splash wave and crater. By t = 0.2s the centre of the vessel contains very little water, with water being located mainly at the outside walls and being thrown out of the vessel due to the extremely high steam production rate.

At the end of the experiment 36% of the water and 13% of the corium were estimated to have been expelled from the mixing vessel. Table 1 shows the amount of melt and water lost at the end of the calculations as a function of melt particle size. The data in Table 1 shows that the prediction of the mass of melt swept-out by the steam is in very good agreement with the experimental data for particles with a diameter in the range 2-3 mm. The mass of water swept-out is too large by a factor of two, but this difference could easily be accounted for by differences between the calculational and experimental geometry.

The calculated integrated mass of steam produced can be used to make a prediction for the pressure transient in the expansion vessel, which is available from the experimental data. The measured pressure rise was small (~ 0.07 MPa) so that the assumption of constant properties, such as steam density and latent heat of vaporisation will not lead to a

significant error. Since the expansion vessel was heated to prevent condensation, the pressure can be estimated by dividing the calculated mass of steam produced by the vessel volume and then by using steam tables to determine the pressure, given the specific volume and temperature. It was assumed that the steam would be rapidly heated to the vessel temperature ($\sim$ 25 K of superheat). Figure 4 shows a comparison of the calculated pressure with the experimental data for a range of particle sizes. The Figure shows that the code predictions for particle sizes of 1, 2 and 3 mm span the experimental data.

The calculated transient steaming rate and the prescribed corium inflow rate are shown in figure 5. The data show that smaller particles lead to more rapid steam generation initially. As large volumes of steam are produced the mixture is dispersed and the steaming rate falls. The second corium inflow causes the steaming rate to increase as more corium enters the system and mixes with the remaining water. The experimentalists [7] obtained a plot of the transient steaming rate against time from the expansion vessel pressurisation data by treating the steam as an ideal gas and differentiating the pressure-time curve to relate $\dot{m}_s$ with $\frac{dp}{dt}$. The present authors believe that this approach is inappropriate, since steam does not behave as an ideal gas close to its saturation temperature and numerical differentiation of such data is notoriously inaccurate. Indeed it seems highly unlikely that the plots shown in Figure 5 could be recovered from the data given in Figure 4. Therefore we believe that the only valid comparison with experimental steam production data is that shown in Figure 4.

To conclude this section on comparison with experimental data we summarise the main features of the simulation:

(i)   The evolution of the system is qualitatively very similar to the experimental observations.

(ii)   The pressurisation of the expansion vessel can be simulated accurately using particle sizes close to those found experimentally.

(iii) Predictions of melt and water 'sweep-out' by steam are in reasonable agreement with the experimental data.

6.2 Application to the Study of Mixing

The motivation for the present work comes from the need to understand steam explosions, which are a mechanism by which the thermal energy of the hot liquid can generate coolant vapour explosively [3]. It is well-established that a necessary precursor to a large-scale steam explosion is the establishment of a coarse mixture of the melt and coolant over a timescale of the order of a second [3].

A key question in this area is, "what is a coarse mixture"? This question can be fully answered only with the help of experimental steam explosion data and the development of physical models of the triggering and detonation processes. Pending the development of such models, we have used physical intuition to construct a quantitative measure of a potentially explosive mixture making use of the currently available information regarding the properties of such mixtures. This is done with the help of an indicator function with carefully chosen properties.

In the context of the present application a good mixture consists of approximately equal volumes of melt and water. In addition, if too much steam is present progression to latter stages of the explosion process is not possible. In general it is also necessary to say something about length-scales of the melt and water but this will be deferred until an evolution equation for length-scales has been developed. Thus consider the following function:

$$\theta(\alpha_S, \alpha_W, \alpha_M) = 16 \ \alpha_M(1-\alpha_M)\alpha_W(1-\alpha_W)f(\alpha_S)$$

where $f(\alpha_S) = \dfrac{1}{1 + X^2}$ (6.1)

$$X = \text{Max}\left((\alpha_S - \alpha_{crit})/\varepsilon, 0\right)$$

$$\varepsilon = 0.05 \ , \quad \alpha_{crit} = 0.6$$

We note that θ has the following properties:

(i) It is symmetric in α_W and α_M.

(ii) It takes values in the closed interval zero to one.

(iii) It achieves its maximum value when $\alpha_M = \alpha_W = 0.5$ and decreases as the mixture becomes lean in either component or as steam is formed.

(iv) The dependence of θ on α_S is such that for $\alpha_S \leqslant \alpha_{crit}$ $f(\alpha_S)$ is

unity and for $\alpha_s > \alpha_{crit}$ the chosen form of $f(\alpha_s)$ ensures that θ is damped smoothly to zero.

We have chosen the simplest functional form for θ satisfying properties (i) - (iv). The chosen values of the parameters α_{crit} and ε are somewhat arbitrary but can be easily modified as better data becomes available. The spatial average of θ, defined by

$$\bar{\theta} = \int_V \theta \; dV \; / \int_V dV \qquad\qquad (6.2)$$

gives a global measure of the degree of mixing.

A series of simulations have been carried out to illustrate the use of the θ function. The same conditions as those described in the previous section were used except there was only a single pour of melt (10.5 kg/s lasting for 0.2s). The increased inflow of melt was achieved by broadening the jet by a factor of three and ensured that there was sufficient melt present to give a visible region of mixture.

Figure 6 shows a plot of $\bar{\theta}$ against time for various conditions which affect vapour production. The base case uses 5 mm melt particles and an ambient pressure of 0.1 MPa. In this situation $\bar{\theta}$ rises to 0.08 at 0.2s and then decreases to 0.05 at 1.0s. Decreasing the particle size to 3 mm changed the initial behaviour only slightly but resulted in a poorer mixture for $t > 0.2s$. This is because smaller particles cause more vapour generation and hence greater dispersion of the melt.

Increasing the pressure to 1.0 MPa causes the volumetric vapour generation to fall allowing better mixing, a phenomenon which has been observed experimentally over this pressure range [11]. Increasing the pressure further to 6.0 MPa causes $\bar{\theta}$ to fall. This is because although only a small volume of vapour is produced a considerable fraction ($\sim 50\%$) of the water is converted to steam, so that there is too little water available for good mixing.

The final calculation is a repeat of the base case but with vapour production artificially supressed. This shows very different behaviour; $\bar{\theta}$ initially increases almost linearly with time for a value of 0.3 at t = 0.6s and then falls as melt and water separate due to buoyancy forces. Because there is no vapour generation there is virtually no loss of melt and water from the vessel and a large region of mixture is formed.

Figures 7 and 8 show the difference between the time evolution of θ for the base case and the isothermal case, respectively. (Contour levels below $\theta = 0.3$ are omitted for clarity.) In the base case steam production causes the melt to be dispersed rapidly as the melt falls through the water pool and there is only a small region of good mixture after the melt reaches the vessel base. In contrast in the isothermal case a large region of mixture is formed both during the fall phase and as the melt reaches the vessel base and spreads up the sidewalls of the vessel.

The above data illustrates the very different behaviour of isothermal and vapour-producing jets. This work strongly suggests that it is

erroneous to model hot melt pouring into water using physical models [12] or correlations [13] which do not take vapour production into account.

7.   Discussion and Conclusions

A 2d finite difference model has been developed to study the evolution of buoyancy-driven, multiphase systems, including the effect of a phase change. Although the numerical scheme is similar to that used in our earlier work [4,5] various modifications and extensions have been made. For example, the velocities of all phases are now calculated simultaneously at each grid node, rather than by using an implicit tridiagonal matrix inversion scheme to relate all the velocities of each species in turn. This practice ensures that Newton's third law is exactly satisfied, produces a very stable numerical scheme, and is computationally cheaper. In addition, an enthalpy equation is solved to determine the melt state (solid or liquid) and temperature, for use in the constitutive relations.

Model predictions have been compared with experimental data for the situation of a jet of hot corium injected into a vessel partially filled with water. The predictions are seen to be in good general agreement with the data for realistic choices for the 'free parameters', even though somewhat arbitrary constitutive relations have been used. This suggests that the empirical relations used to model interphase drag and heat transfer must be at least of the correct order of magnitude. Work is in progress to improve the modelling in this area (see below). Many of the qualitative features of the numerical simulations faithfully reproduce experimentally observed phenomena. Furthermore, these features are

relatively insensitive to the specifics of the constitutive relations. Simulations have also been carried out to show the difference between the mixing of an isothermal and a vapour-producing jet injected into a pool of a different fluid. A quantitative description of a mixture (in the context of steam explosion research) has been proposed and clearly demonstrates the different evolution of the two systems.

It is intended to extend the present work by developing evolutionary equations for the component length-scales so that features such as droplet break-up and reagglomeration can be modelled. In addition, improved constitutive relations are being sought. Further experimental comparison will be carried out as suitable data become available and the model will be used in a predictive capacity to determine the most important geometrical and external factors affecting mixing.

8. Acknowledgement

References

1. Long, G., Explosions of molten metal in water - causes and prevention. Metals Progress, 71, p.107-112 (1957).

2. Colgate, S.A., and Sigurgeirsson, T., Dynamic mixing of water and lava, Nature, 244, p.552-555 (1973).

3. Gittus, J.H.(Ed.), Report on PWR Degraded Core analysis, UKAEA report NDR-610(s), Chapter 5, 1982.

4. Thyagaraja, A., Fletcher, D.F. and Cook, I., One dimensional calculations of two-phase mixing flows. Culham Laboratory report CLM-P770 (1986). (Accepted for publication in Int. J. Num. Meth. Eng.).

5. Fletcher, D.F., and Thyagaraja, A., Numerical Simulation of One-dimensional multiphase mixing. Culham Laboratory report CLM-P776 (1986).

6. Harlow, F.H., and Amsden, A.A., Flow of interpenetrating material phases. J. Comp. Phys., 18, p.440-465 (1975).

7. Spencer, B.W., McUmber, L., Gregorash, D., Aeschlimann, R. and Sienicki, J.J., Corium quench in deep pool mixing experiments. Paper presented at National Heat Transfer Conference, Denver, Colorado, USA, 4 August, 1985. (CONF-850810-10)

8. Witte, L.C., Film boiling from a sphere, I & E C Fundamentals, $\underline{7}$, p.517-518 (1968).

9. Wallis, G.B., One-dimensional two-phase flow, McGraw-Hill, New York (1981).

10. Fletcher, D.F., The particle size distribution of fragmented molten fuel coolant interaction debris. UKAEA Winfrith report AEEW-M2103, (1984).

11. Bird, M.J., An experimental study of Scaling in core melt/water interactions. Paper presented at the 22nd National Heat Transfer Conference, Niagara Falls, 5-8 August, 1984.

12. Theofanous, T.G. and Saito, M., An assessment of class-9 (core melt) accidents for PWR dry containment systems. Nucl. Eng. & Design, $\underline{66}$, p.301-332 (1981).

13. Corradini, M.L., Molten fuel/coolant interactions: recent analysis of experiments. Nucl. Sci. and Eng., $\underline{86}$, p.372-387 (1984).

Melt particle size (mm)	% of melt lost	% of water lost
1	40	85
2	18	67
3	9	62

Table 1: The effect of particle size on
melt and water 'blow-off'.

Fig.1. The finite difference mesh.

To expansion tank
(volume 1·4 m³)

Melt inflow
(22 mm diameter jet)

Interaction vessel
(212 mm ID × 510 mm high)

Expansion pipeway
(108 mm ID)

Water pool
320 mm deep
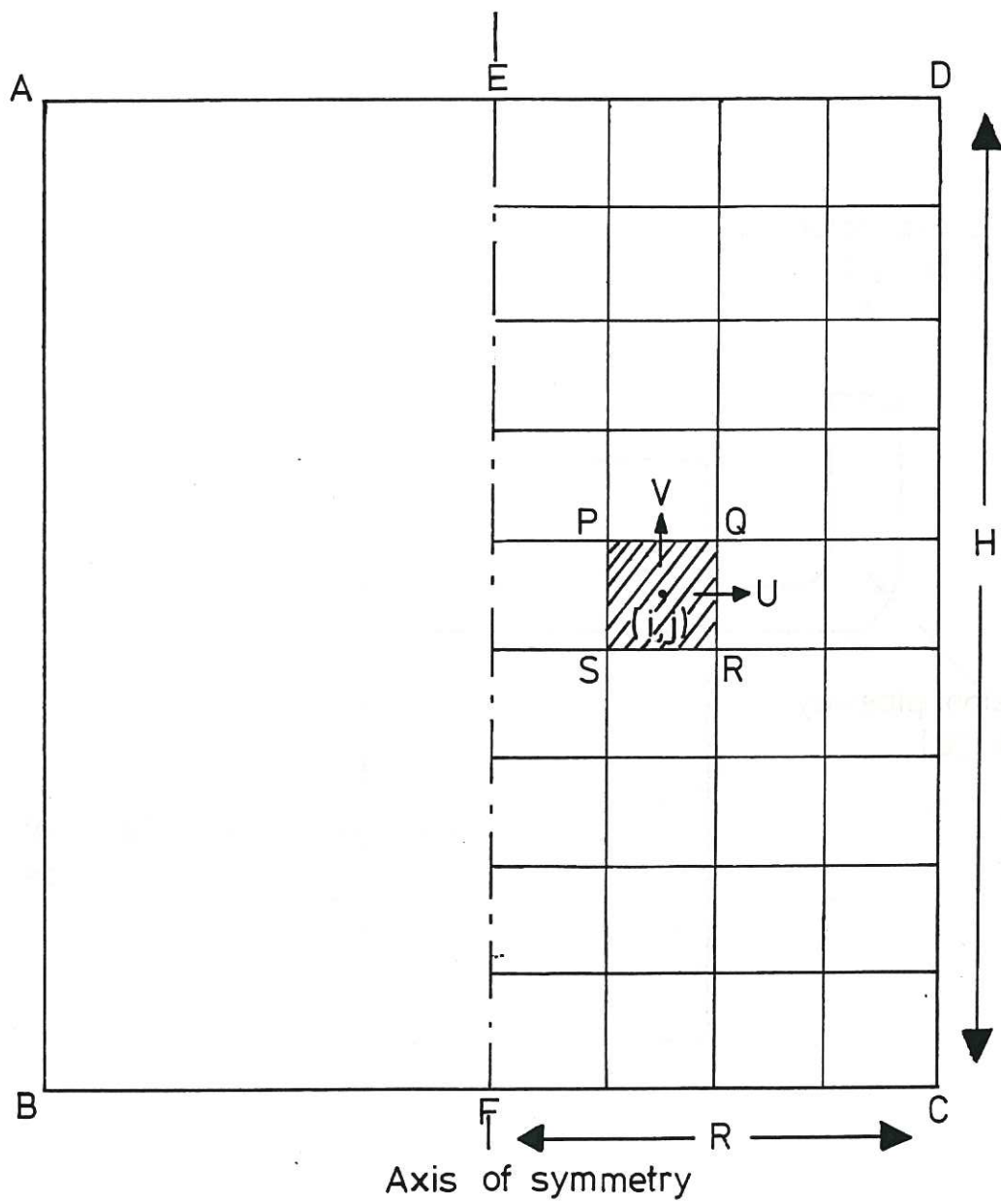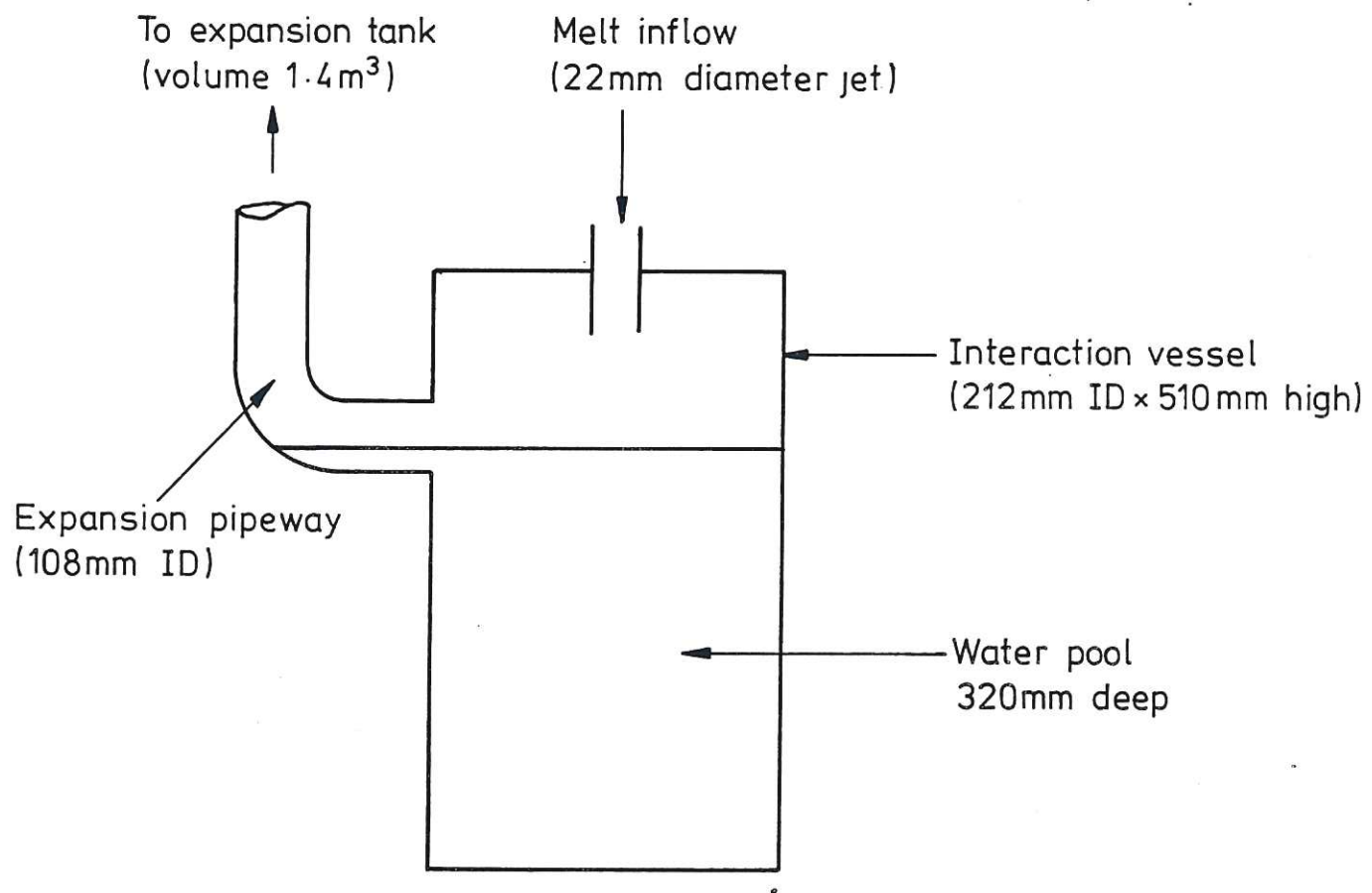
Fig 2. Illustration of the experimental geometry

MELT VOLUME FRACTION

WATER VOLUME FRACTION

STEAM VOLUME FRACTION
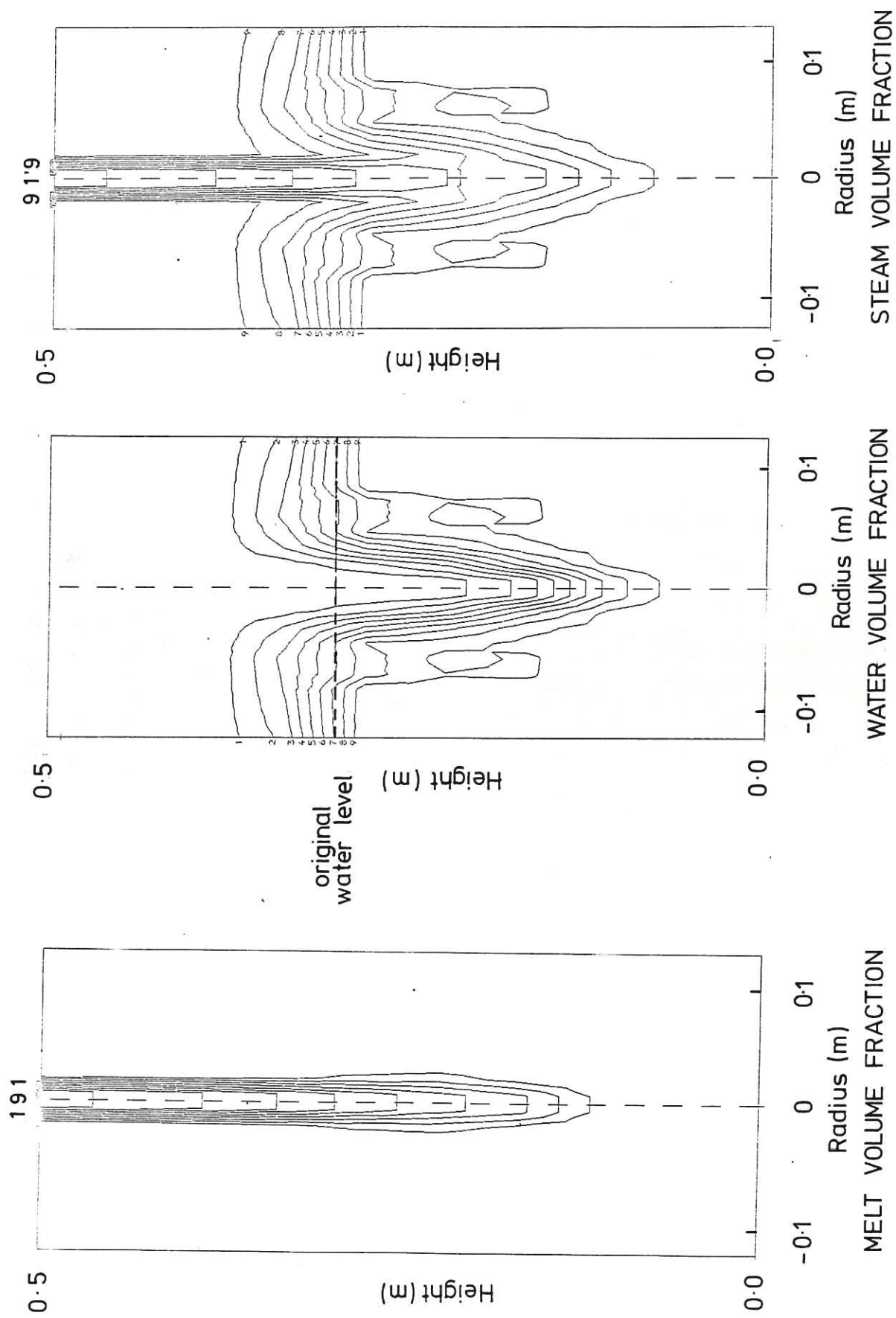
Contour level 1 = 0·1 increasing in steps of 0·1

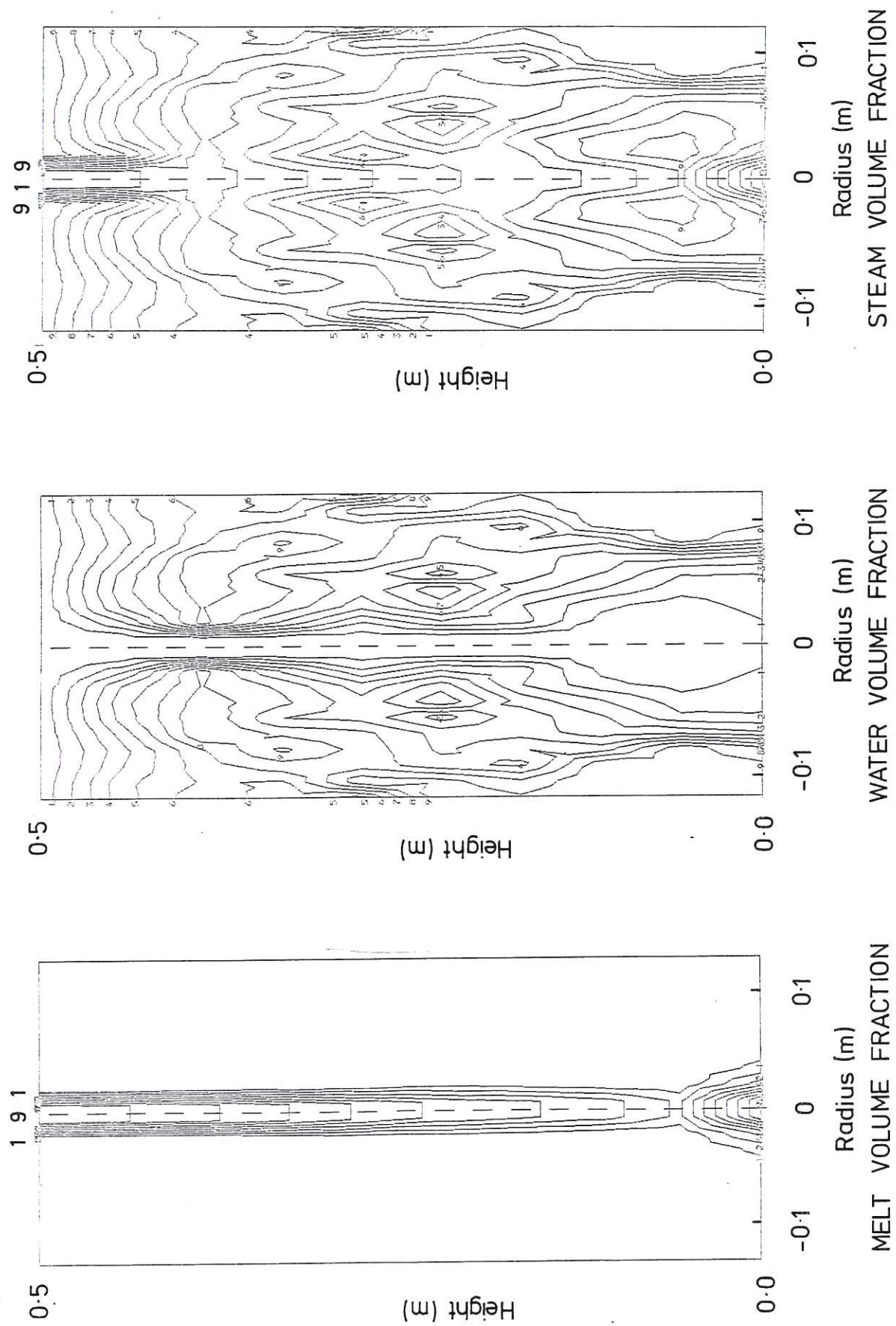Fig. 3(a). Volume fraction distribution at t = 0·1s for 2mm particle case

MELT VOLUME FRACTION   WATER VOLUME FRACTION   STEAM VOLUME FRACTION

Contour level 1=0·1 increasing in steps of 0·1

Fig. 3 (b). Volume fraction distribution at t=0·2s for 2mm particle case
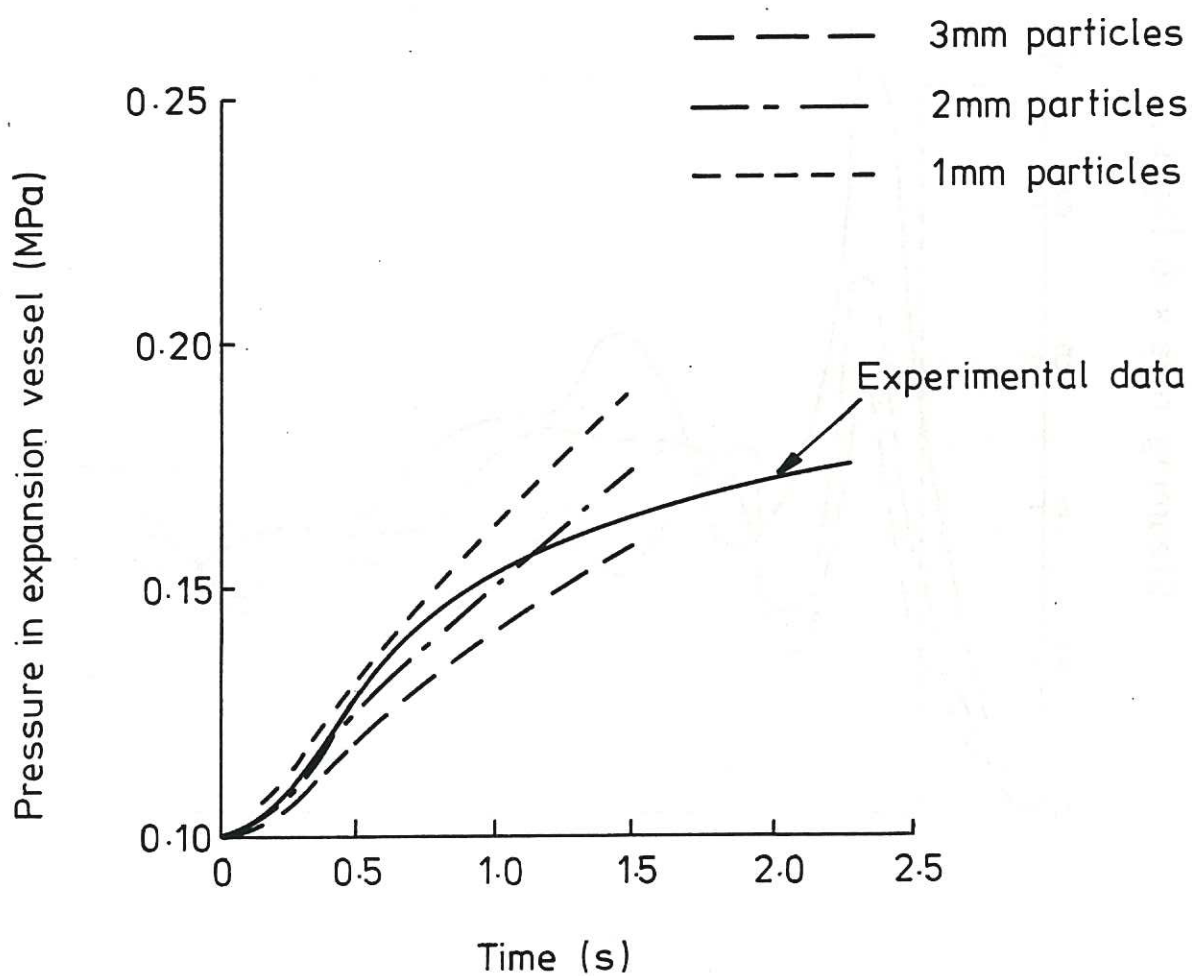
Fig 4. A comparison of the predicted
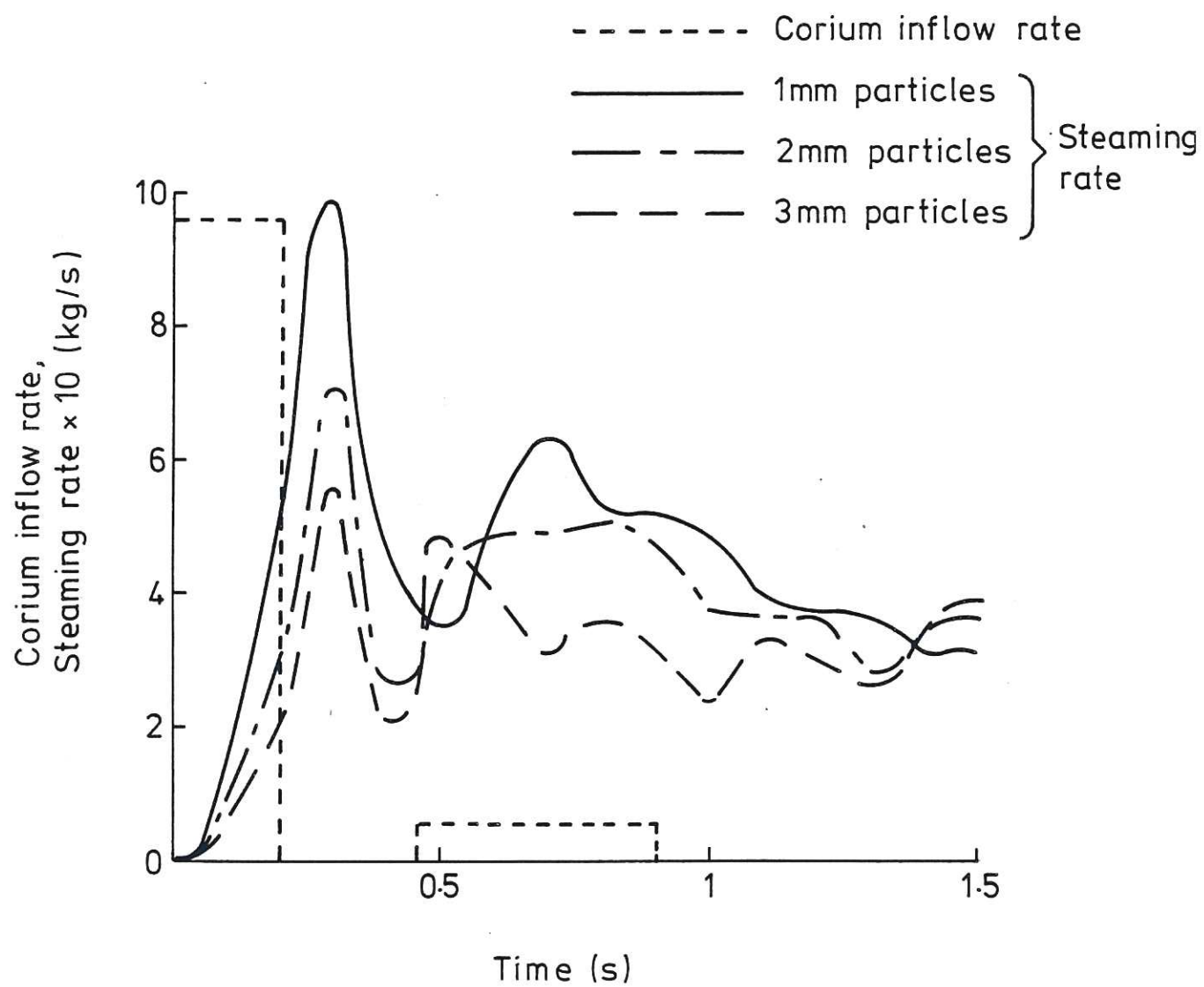and measured vessel pressurisation data

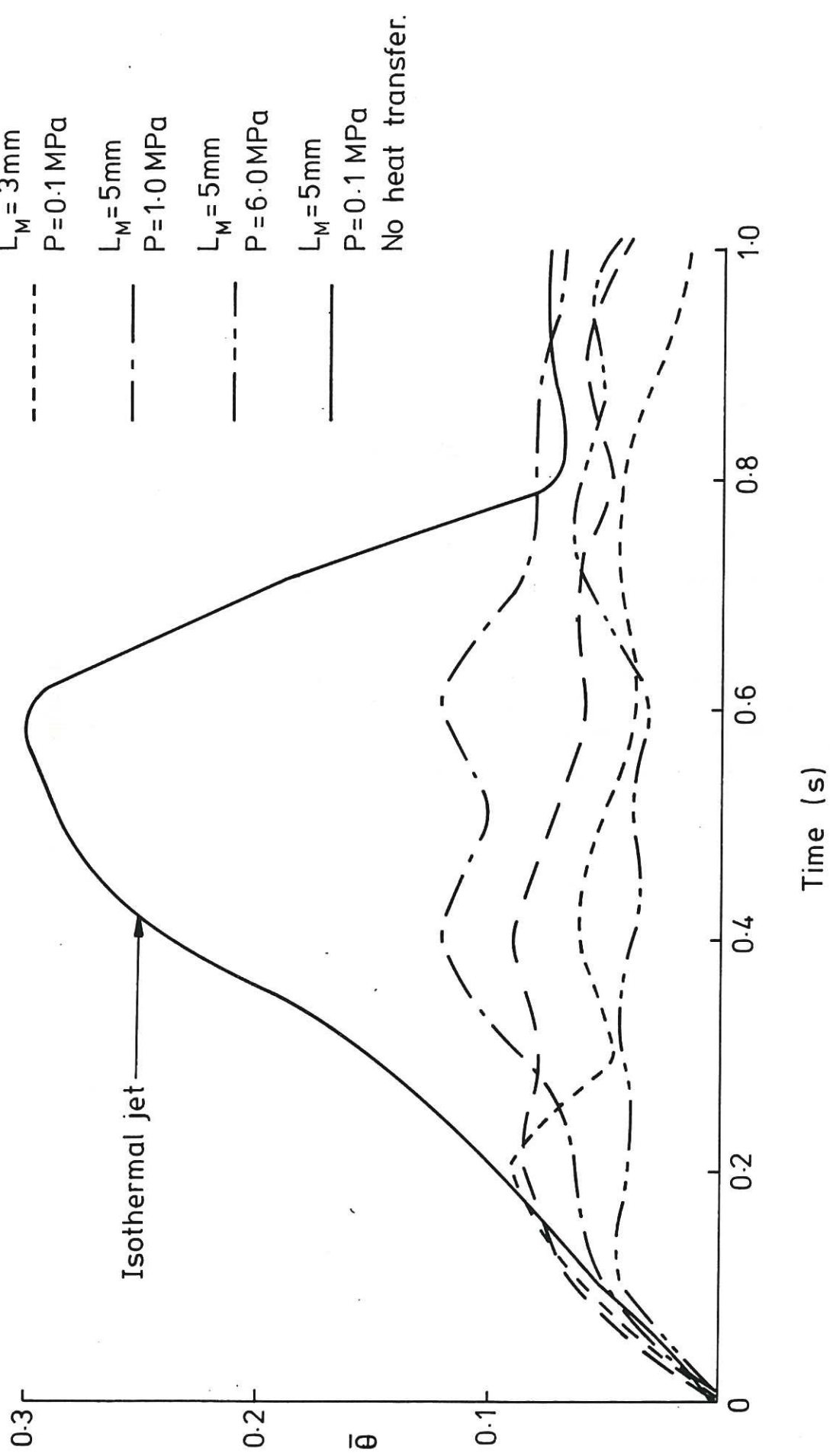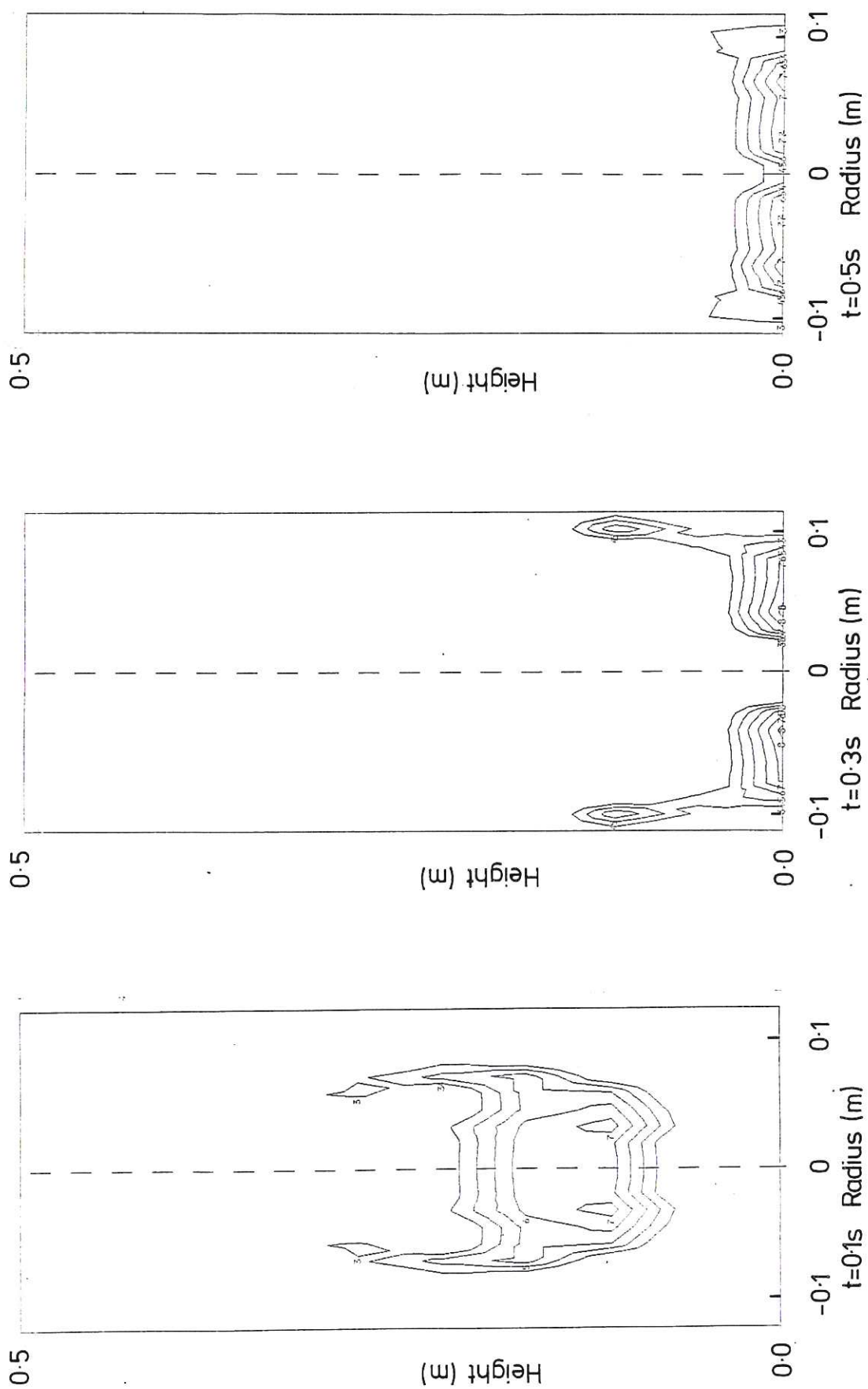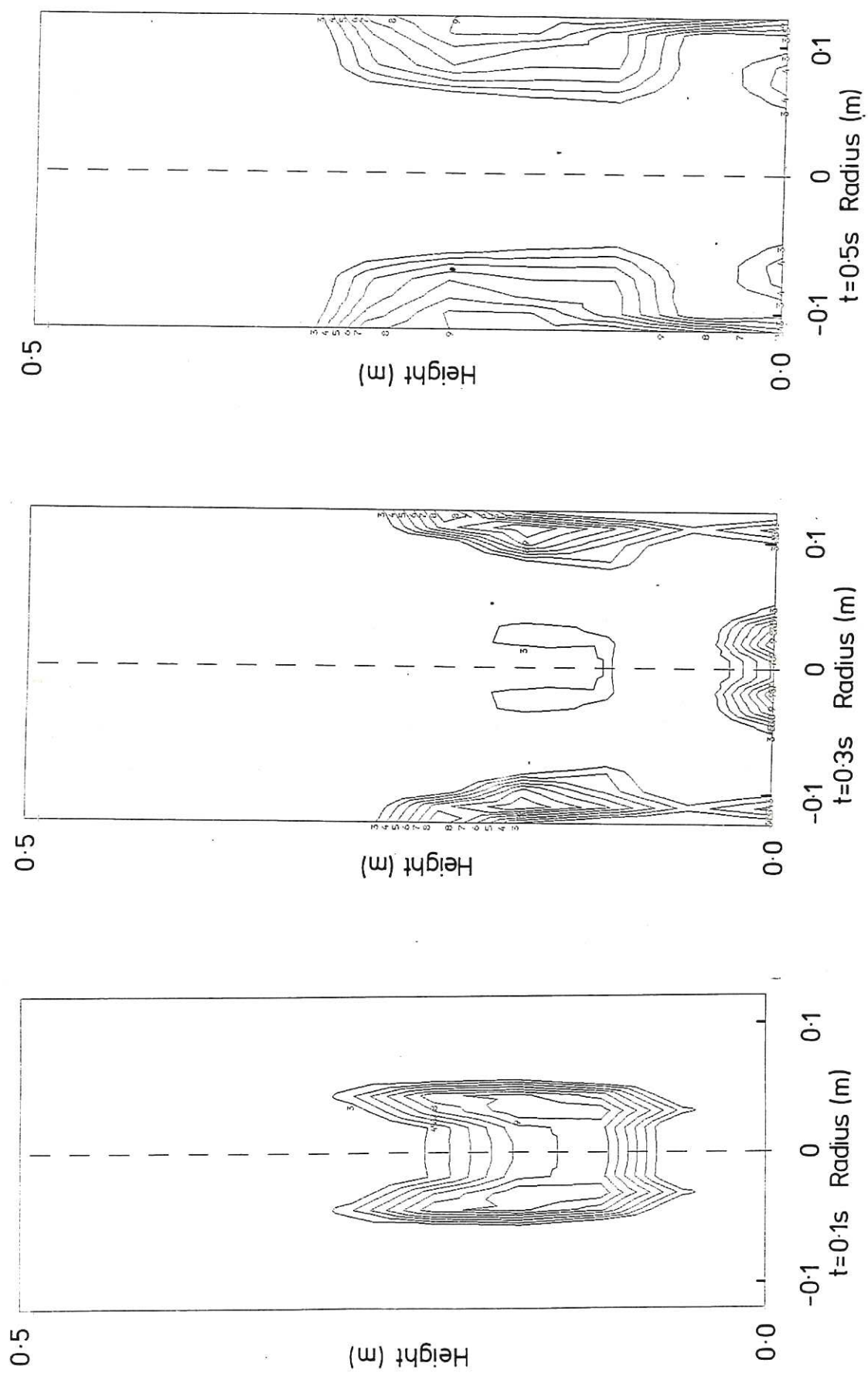Fig 5. The transient steaming rate as a function
of particle size

Fig 6. The effect of vapour production on mixing

Legend:

$L_M = 5mm$
$P = 0.1\,MPa$
— —

$L_M = 3mm$
$P = 0.1\,MPa$
- - -

$L_M = 5mm$
$P = 1.0\,MPa$
— · —

$L_M = 5mm$
$P = 6.0\,MPa$
— ·· —

$L_M = 5mm$
$P = 0.1\,MPa$
No heat transfer.
———

Isothermal jet

Time (s)

$\bar{\theta}$

0.3

0.2

0.1

0   0.2   0.4   0.6   0.8   1.0

(Contour level 3 represents θ=0·3 etc)

Fig.7. θ contours for the base case calculation

(Contour level 3 represents θ = 0·3 etc)

Fig.8. θ contours for the isothermal jet case